Materials Science & Engineering A 678 (2016) 291–298

Contents lists available at ScienceDirect

Materials Science & Engineering A

journal homepage: www.elsevier.com/locate/msea

Neutron diffraction measurements of residual stress in additively manufactured stainless steel

D.W. Brown*, J.D. Bernardin, J.S. Carpenter, B. Clausen, D. Spernjak, J.M. Thompson

Los Alamos National Laboratory, Los Alamos, NM 87545, USA

ARTICLE INFO

Keywords:
Additive manufacture
Neutron diffraction
Residual stress

ABSTRACT

Charpy test specimens were additively manufactured (AM) on a single stainless steel plate from a 17–4 class stainless steel using a powder-bed, laser melting technique on an EOS M280 direct metal laser sintering (DMLS) machine. Cross-hatched mesh support structures for the Charpy test specimens were varied in strut width and density to parametrically study their influence on the build stability and accuracy as the DMLS process has been known to generate parts with large amounts of residual stress. Neutron diffraction was used to profile the residual stresses in several of the AM samples before and after the samples were removed from the support structure for the purpose of determining residual stresses. The residual stresses were found to depend very little on the properties of the support structure over the limited range studied here. The largest stress component was in the long direction of each of the samples studied and was roughly 2/3 of the yield stress of the material. The stress field was altered considerably when the specimen was removed from the support structure. It was noted in this study that a single Charpy specimen developed a significant tear between the growth plate and support structure. The presence of the tear in the support structure strongly affected the observed stress field: the asymmetric tear resulted in a significantly asymmetric stress field that propagated through removal of the sample from the base plate. The altered final residual stress state of the sample as well as its observed final shape indicates that the tear initiated during the build and developed without disrupting the fabrication process, suggesting a need for *in-situ* monitoring.

1. Introduction

Additive manufacture (AM) refers to the process of “growing” parts to near net-shape using a bottom-up methodology through deposition of material from either powder or wire feed. This is in contrast to the more traditional top-down fabrication methodology that involves subtractive techniques where material is removed from cast or wrought billets to achieve a particular geometry. Powder-bed AM processes for metals, in particular, often exhibit strong thermal gradients and rapid quenching of the deposited material. These necessarily result in large, often yield-level, residual stresses [1] in the as-deposited part which can result in premature fracture if the part remains on the build substrate or large-scale distortions when removed from the substrate.

The use of support structures during powder-bed based metal AM fabrication is ubiquitous. The support structure is used to control heat transfer between the part and the base plate and constrain the part during manufacturing. The support is a hatched porous structure, where the hatching parameters (cell size and porosity) are considered important manufacturing parameters affecting the residual stresses. After fabrication has finished, the support structure and base plate are removed from the final part through subtractive machining techniques. Due to the expense of feedstock material and the time associated with fabrication, studies have focused on the minimum density needed for a successful support structure [2,3]. In addition to looking at density, other studies have focused on the shapes and spacing of the struts that form support structures [4,5] These studies have generally focused on geometric stability of the final part after removal of the support structure and base plate. No study, however, has quantified measures of the stress state within parts prior to and after removal from the base plate as a function of support structure.

The obvious need has motivated several residual stress measurements in additively manufactured samples using, for instance mechanical relaxation techniques (*e.g.* crack-compliance [1]) as well as x-ray [1,6,7] and neutron diffraction techniques [8–11]. Neutron diffraction is particularly relevant because neutrons penetrate bulk distances (cm's) into most structural materials [12], *e.g.* steel, copper, nickel, *etc*, allowing for non-destructive mapping of multiple stress components at depth in an AM part. Moreover, the non-destructive nature of neutron diffraction allows for evolutionary measurements of residual stress in the same part after multiple processing steps, e.g [13], such as

* Corresponding author.

http://dx.doi.org/10.1016/j.msea.2016.09.086
Received 9 August 2016; Received in revised form 19 September 2016; Accepted 20 September 2016
Available online 22 September 2016

before and after an AM part is removed from the substrate, or before and after hot-isostatic pressing. The advent of high energy synchrotron x-ray sources (> 60 keV), such as the 1ID beamline [14] at the Advanced Photon Source (APS), also offers the ability to non-destructively map stresses at depth. However, due to the low diffraction angle associated with high energy x-ray diffraction, it is often difficult to determine through-thickness stress components in 3-dimensional parts and one must often extrapolate, resulting in increased uncertainty [15]. A drawback of both neutron and synchrotron based diffraction measurements of residual stress is that access to the required instrumentation is extremely limited. Thus, the best usage of the limited access to the relevant beamlines is to couple the residual stress measurements with computational modeling (often finite element analysis) to provide validation of the model, which can then be used to predict and optimize the final properties (*e.g.* residual stress) in parts as a function of input parameters.

In this study, several samples with a Charpy test geometry [16] were additively manufactured on a solid base plate with mesh support structures varied in order to control the conduction of the heat and the mechanical constraint of the sample. The Charpy test specimen geometry was convenient and added a feature (the notch, grown perpendicular to the base plate) which could potentially alter the residual stress profile. Neutron diffraction was used to profile the lattice parameter of the AM samples with spatial resolution both before and after removal of the samples from the sub-structure. The residual stresses were determined from the variation of the observed lattice parameter from a reference value.

2. Experimental

2.1. Sample preparation

The thickness of the part and mostly uniform cross sectional area make the Charpy specimen geometry suitable for neutron-based scoping experiments on thick z-axis parts. 10 mm tall rectilinear block style support structures were generated as separate STL (standard tessellation language) files consisting of cell hatchings ranging from 0.25 to 0.6 mm and populating 0.3 mm fragmentations in increments ranging from 3 mm to 5 mm. The support height and other fixed variables were determined *via* a down-selection process based on several preliminary tests exploring upper and lower bounds for key parameters.

Overall, 14 samples with Charpy geometry (labeled A-N) were grown on a single square stainless steel plate (252 mmx252 mm) for multiple purposes, including these residual stress measurements. Fig. 1(a) shows a schematic of the build plate, Fig. 1(b) a schematic of an individual sample, including the coordinate system used in this paper. The specimens were grown in a single build using a powder-bed, laser melting technique on an EOS M280 direct metal laser sintering (DMLS) machine. The hatching (h) and fragmentation (f) of the support structure were varied across the 14 samples in a controlled manner to monitor their influence on the final sample. The base plate was sectioned between individual specimens to allow passage of the neutron beam (neighbor specimen would have interfered). After completion of residual stress measurements on the as-built specimens, they were removed from the base plate and mesh sub-structure using a cut off wheel and a subset of the residual stress measurements were repeated on the free specimens.

Table 1 lists different parameters which were varied in the growth of the samples studied here-in. Neutron diffraction based residual stress measurements were completed on four of the Charpy samples; A, C, D, and K. Pictures of Samples A and C mounted in the diffractometer are shown in Fig. 2(a) and (b) Samples A and C were constructed with the same support structure parameters, h=0.25 and f=3, while D and K had distinct parameters, h=0.25, f=5 and h=0.35 and f=4, respectively. Sample A was intentionally grown closer to the edge of the plate than is typically done, 26.7 mm from the edge, while C was grown closer to the center, 80.2 mm from the edge, to study the effect of the altered heat flow at the edge..

Significant separation of the support structure of Sample A from the build plate was observed, see Fig. 2(b) The tear occurred on the side of the sample nearest the lateral edge of the plate and furthest along the direction of travel of the recoat blade as highlighted in Fig. 1(a) This single observation in Sample A is not sufficient to concluded that the growth position near the top of the plate, which alters the heat flow, is the definitive cause of the tear between the growth plate and mesh sub-structure. A stochastically occurring defect could equally well have been the cause. However, we note that Sample H (not studied further here-in) was the only other sample to manifest such a tear and it was grown in a position symmetrical to A.

A 3.5 mm cube was cut from Sample J, made with parameters identical to A and C, to be used as a reference lattice parameter, a_0, measurement. Compression and tension samples were EDM'ed from two of the samples, B and J to determine the macroscopic strength properties of the as-deposited material. The compression specimen was a cylinder 6.3 mm in diameter by 15 mm long. The tension sample was a threaded end specimen, ASTM E8 – 04 (Sub-size Round Tension Test Specimen) with a 3 mm diameter in the gauge length.

A FARO Edge HD Laser Line Probe was used to scan the surface geometry of sample M before and after removal from the base plate in

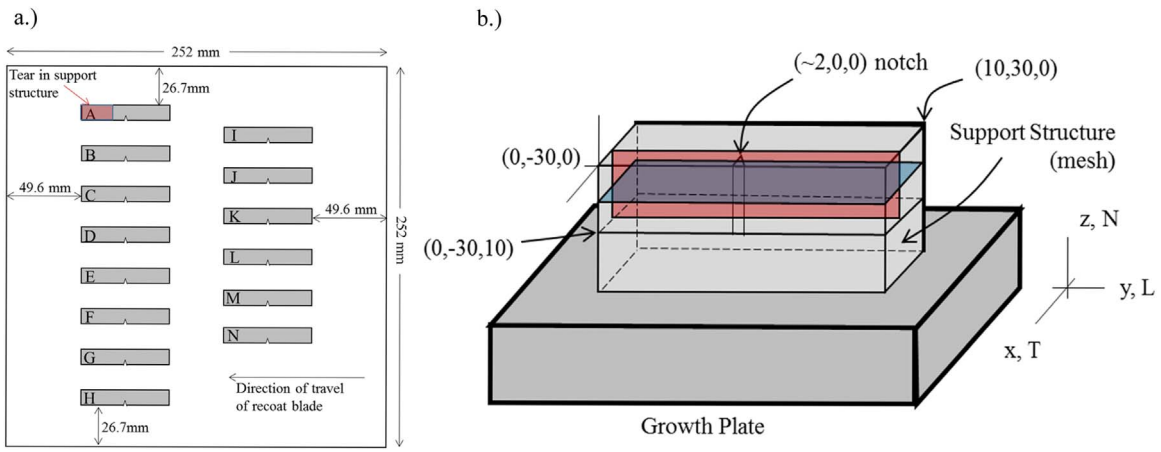

Fig. 1. (a) Schematic (roughly to scale) of build with 14 Charpy specimen. (b) Schematic of individual sample showing coordinate system and measurement loci discussed in the text. All units in mm. The origin (0,0,0) is at the top of the front face at the center length as shown, putting the tip of the notch at roughly (2, 0, 0) mm. (For interpretation of the references to color in this figure legend, the reader is referred to the web version of this article.)

Table 1
Support structure parameters and build plate location for the Charpy specimens used in this work..

Sample growth position (edge)	A Near	B Far	C Far	D Far	J Far	K Far	M Far
Sub-structure Hatching (mm)	0.25	0.25	0.25	0.25	0.25	0.35	0.3
Sub-structure frag. (mm)	3	3	3	5	4	4	4
Use	Residual stress	T. sample	Residual stress	Residual stress	C. Sample and d0 cube	Residual stress	Distortion

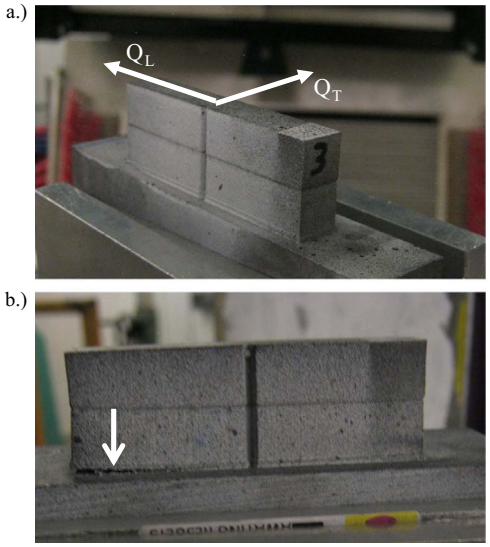

Fig. 2. (a) and (b) Pictures of samples C and A, respectively, as mounted on SMARTS. The white arrows in (a) represent the longitudinal (L) and transverse (T) diffraction vectors defined by the instrument geometry. The tear between the substructure and the growth plate is indicated by the white arrow.

order to quantify the distortion of the specimen due to the relaxation of the residual stresses. The laser has a scan rate of 280 feet/sec and captured 2000 individual points for every scan line of data. The resulting point cloud was imported into Polyworks© and aligned to the original and ideal CAD file geometry model *via* a best fit approach.

2.2. Neutron diffraction measurement of stress

The residual stress measurements were completed on the Spectrometer for Materials Research at Temperature and Stress (SMARTS) diffractometer at the Los Alamos Neutron Science Center (LANSCE), at Los Alamos National Laboratory. The residual stress samples were mounted on the SMARTS translator table and aligned with respect to the center of the diffractometer using computerized theodolytes. SMARTS is a time-of-flight (TOF) diffractometer, with a continuous incident energy spectrum peaked at ~1.5 Å, but usable at wavelengths from 0.7 to 5.5 Å [17]. The cross section of the incident beam was defined by 2 mmx2 mm boron nitride apertures. Two detector panels are located at ± 90° from the incident beam and span ± 13° in the vertical and horizontal planes. Because the incident neutron beam has a continuous energy spectrum, each detector panel records an entire diffraction pattern (d-spaces from 0.5 to 4 Å) simultaneously and with parallel diffraction vectors bisecting the incident and diffracted beam vectors, i.e. at ± 45° from the incident beam. Each detector is focused by a radial collimator to accept neutrons from a 2 mm section along the direction of the beam. The crossover of the incident beam and field of view of the radial collimators defines an 8 mm^3 "gauge" volume from which the diffraction data is collected and over which average lattice parameters are determined.

When the sample growth direction was vertical, as is shown in Fig. 1(a), the two banks recorded the transverse (+90° bank) and longitudinal (−90° bank) strains and when it was horizontal the growth (normal) (+90° bank) strains were recorded. The sample was swept through the gauge volume by a motorized translator table and diffraction patterns collected as a function of position in the sample. The neutron diffraction collection times were ~15 min per point.

The lattice parameter, effectively averaged over the gauge volume, was found by Rietveld refinement of the observed diffraction pattern using the General Structural Analysis Software (GSAS) developed at Los Alamos [18]. A reference lattice parameter (a_0) was determined from a small (3.5 mm) cube section from a sister sample such that macroscopic residual stresses were released. The strain is determined from the variation of the lattice parameter relative to the reference

$$\varepsilon_a = (a - a_0)/a_0. \quad (1)$$

Then, stress is determined from Hooke's Law,

$$\sigma_i = \frac{E}{(1+\nu)(1-2\nu)}[(1-\nu)\varepsilon_i + \nu(\varepsilon_j + \varepsilon_k)], \; i,j,k \in L, T, N \quad (2)$$

where L, T, and N refer to the longitudinal, transverse and normal components, respectively, and E and ν are the bulk Young's modulus and Poisson's ratio, taken to be 190 GPa and 0.27, respectively. This calculation assumes that the measured normal strain components are representative of the bulk behavior and that the material is isotropic [19]. However, it is important to note that unless the measured normal strain components are indeed the principal strain components at the given location, neither the measured strain components nor the calculated stress components are representative of the full strain or stress *tensor* at the given location. The stresses so determined are still accurate, they just do not represent the principal stress components if the adopted coordinate system is not the principal coordinate system. To determine the full strain and stress tensors without *a priori* knowledge of the principal directions a minimum of six independent strain components must be measured [20] to account for the presence of any shear strain components that cannot be measured directly *via* diffraction.

The uncertainty in the measurement of the residual strain is between 25 and 40 με (estimated standard deviation), depending on the length of the path the neutrons had to travel through the sample material, resulting in uncertainties in stress of ~10–15 MPa. Other sources of uncertainty, such as local variations of chemistry or changes in crystallographic texture which can change the effective elastic modulus, have been ignored.

Fig. 1(b) shows a schematic of an individual sample with the origin and directions, L, T, and N, defined. The colored planes represent the loci of stress profiles completed on the samples. Full residual stress profiles were completed over a y-z plane (x=3.8 mm) shown in red schematically in Fig. 1(b) on Samples A and C, before and after being parted from the sub-structure. The y-z stress profile was repeated on Samples A and C following removal from the growth plate. Because they were very similar to Sample C, only L and T residual strains were measured on the same plane in Samples D and K before separation, for the sake of beam time. Also, the residual stresses were profiled over an x-y plane (z=5.0 mm) shown in blue in Fig. 1(b) on Sample C, while still attached to the base plate.

3. Results

3.1. Macroscopic response

Fig. 3 shows the macroscopic flow curves of the as-deposited material during tensile and compressive deformation. The drops in stress occur when the tests were interrupted and held at constant cross head displacement while neutron diffraction data were collected. The results of the in-situ diffraction will be discussed in a future publication; only the macroscopic properties are presented here. The material initially deforms elastically with a modulus of 190 ± 10 GPa before yielding at roughly 600 MPa. Initially little hardening, or even softening, is observed with strain beyond the yield point. During both tensile and compressive deformation, the material begins to harden significantly beyond a true strain of roughly 0.06. While the compression test was halted at a true strain of 0.08, in tension the flow stress of the as-deposited material continued to increase, reaching 1200 MPa at a tensile strain of 0.12. These properties are consistent with those published by the material provider [21]..

3.2. Lattice parameter variation

The as-deposited material was single phase austenitic steel (face-centered cubic) to our measurement resolution (roughly 1% volume fraction). Several profiles of the lattice parameters as a function of the longitudinal distance (y) along the sample axis will be shown in what follows. Note that the color scheme and, more importantly, the absolute scale of the ordinate is held fixed throughout all of the lattice parameter profiles.

Fig. 4(a)–(c) show longitudinal (y–) line profiles of the lattice parameters in the L, T, and N directions, respectively, on the x-y plane at z=5.0 mm at incremental values of x in Sample C. The blue plane in the inset in Fig. 4(c) highlights the locus of measurement points on the sample (lines color matched to the plots). Note, there is no measurement at x=2.1 mm and y=0 mm because there is no material at the notch location. Also, the x=8.0 mm line is lacking two points due to beam time considerations. The value of the reference lattice parameter, a_0=3.5970 ± 0.0002 Å, is indicated by the solid black line. A lattice parameter variation corresponding to 0.1% elastic strain is also indicated..

There is a relatively small effect of the notch on the profile of the L-direction lattice parameter that passes through the notch (i.e at x=2.1 mm). Otherwise, the lattice parameter in the L direction is independent of x; it is peaked near the center length (y=0 mm) and a minima near the ends (y= ± 30 mm). The lattice parameter in the transverse and normal directions show relatively less dependence on position along the length (y), but tend to increase as the profile line moves away from the notched side (i.e. with increasing x). A sharp increase in the N-direction lattice parameter is observed on the x=2.1 mm line very near the notch.

Fig. 5(a)–(c) show similar longitudinal (y-) line profiles of the lattice parameters in the L, T, and N directions, respectively, on the y-z plane at x=3.8 mm at incremental values of z. The red plane in the inset in Fig. 5(c) highlights the locus of measurement points on the sample (lines color matched to the plots). Again, the value of the reference lattice parameter, a_0, is indicated. Fig. 5(a) shows L-direction lattice parameters from Samples C (solid circles), D (open circles), and K (x's). Recall that Samples C, D, and K were built on sub-structure meshes with differing hatching and fragmentation. The agreement of the L lattice parameters observed in the three samples, C, D and K, is remarkable. Similar agreement of the T lattice parameters between Samples C, D and K was observed. There is relatively little spatial variation of the T-direction lattice parameter. Thus, Fig. 5(b) shows only the results from sample C, as plotting the results from all three samples greatly obscures the plot. Finally, because real time data analysis during the experiment indicated that there was little variation between the three samples, the N-direction lattice parameter was only measured in Sample C, in the interest of beam time, and is shown in Fig. 5(c)..

The lattice parameter in the L-direction shows by far the strongest variation. Near the ends of the specimen (y= ± 30 mm), the lattice parameters observed in the L-direction are near the reference lattice parameter, independent of z, as should be expected when approaching a free surface. At the center length of the specimen, the L-direction lattice parameter depends strongly on z. Near the interface with the mesh sub-structure (z=10 mm), the L-direction lattice parameter is a local minimum, while near the free surface (z=0 mm), it is a local maximum. There is relatively little variation of the lattice parameter in the T and N direction. The T direction lattice parameter is nearest the reference value near the top and bottom of the sample (z=2 and 7.9 mm) and decreases in the middle. The N-direction lattice parameter does show an interesting spike near the center length (y=0 mm) as well as at the ends on the side opposite the notch (x=7.9 mm).

Fig. 6(a)–(b) compare the L-direction lattice parameters observed on the same y-z plane (x=3.8 mm) in Samples C and A while still attached to the growth plate. The T- and N-direction lattice parameters are omitted for brevity. Recall that Samples A and C were grown with the same sub-structure parameters, but A was nearer the edge of the growth plate and a significant tear developed between the sub-structure and the base plate under Sample A during the deposition of the sample. Again, the red plane in the inset in Fig. 6(c) highlights the locus of measurement points on the sample (lines color matched to the plots) and the location of the tear in Specimen A is roughly represented by the yellow plane. The tear in Specimen A clearly results in a very different lattice parameter profile from that observed in Sample C. The lattice parameter profile is significantly asymmetric in Sample A. Specifically, over the tear, the lattice parameter in the L direction reaches an absolute minima..

Fig. 6(c)–(d) show the same measurements repeated after the samples have been parted from the sub-structure and growth plate. In both samples, the lattice parameter changes significantly when the constraint of the sub-structure is removed. The asymmetry apparent in the lattice profile of Sample A remains following separation from the base plate.

Fig. 7(a) and (b) show displacements of the top surface of an identical sample (M) from the original and ideal CAD file geometry before and after removal from the base plate, respectively. The color contour map of the point displacements show that the Charpy specimen was curled up slightly in the shape of an open “C” after the build. The distortion of the sample from ideal increased significantly once it

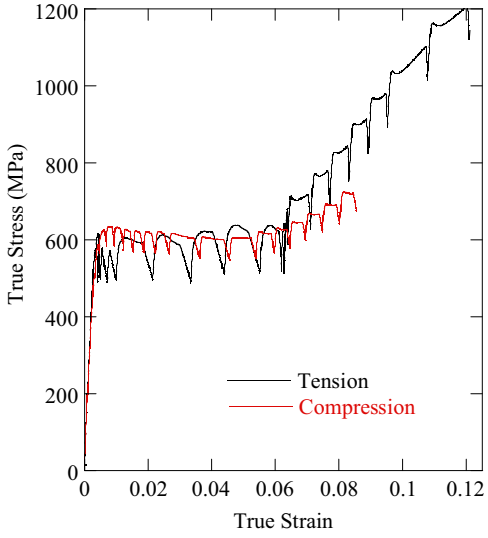

Fig. 3. Stress-strain curves of as-deposited GP-1 in tension and compression.

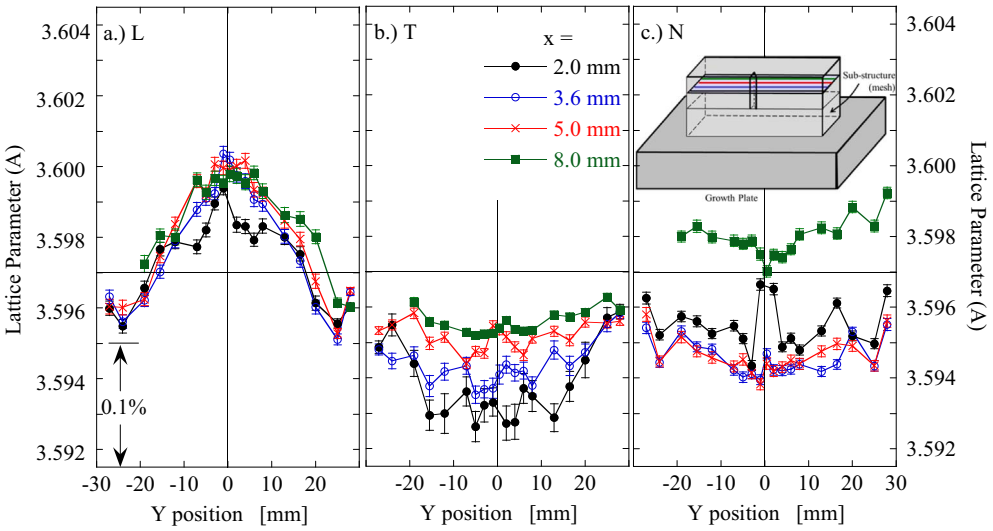

Fig. 4. (a)–(c) Longitudinal (y) line profiles of L, T, and N-direction lattice parameters on an x-y plane (at z=5.0 mm) at increasing values of x in Specimen C. The inset schematic in (c) highlights the locus of measurement points (colors matched to plots) on the specimen. (For interpretation of the references to color in this figure legend, the reader is referred to the web version of this article.)

was removed from the support material and base plate, that is once the mechanical constraint was removed. The peak (ends) to valley (center) distortion is 0.26 mm. Also, the depression is broader and deeper on the side away from the notch..

4. Discussion

Fig. 8 shows the L, T, and N components of the residual stresses profiled on the x-y plane (z=5 mm, blue plane in Fig. 1(b) in Sample C while still attached to the substructure. The presence of the notch results in a significantly asymmetric stress field in this plate. The absence of material at the notch significantly alters the L stresses on that side of the sample. Near the center length of the sample (−20 mm < y < 20 mm) on the notch side, the L stress is roughly −100 MPa compressive, except for a slightly tensile spike very near the notch. In contrast, the L stress on the back side of the sample is tensile and roughly 150 MPa. The T and N stress show similar variation due to the presence of the notch. This stress profile is expected since the notch acts like a stress relief on the x=0 mm side of the part, resulting in a compressive or near zero stress field. On the opposite side (x=10 mm), the part is attempting to coil inward but remains constrained by the continuous support structure, and thus a highly tensile stress is created..

Fig. 9(a) shows the L, T, and N components of the residual stresses profiled on the y-z plane (x=3.8 mm, red plane in Fig. 1(b) in Sample C while still attached to the substructure. The L stress is large (roughly 400 MPa) near the free surface (z=0 mm) at the mid-length of the part (y~0 m) and symmetrically approaches zero as the free ends (y= ± 30 mm). A large bending moment (the top is in tension ~400 MPa, bottom in compression, −300 MPa) is evident in Sample C when still attached to the build plate as seen in Fig. 9(a). The neutral axis is shifted away from the center height (z=5 mm) of the sample due to the constraint from the substructure. The T and N stresses are both compressive except near the top surface, where they are close to zero..

The observed stress profile is expected based on the final thermal gradient experienced by the sample during deposition. Hot material is

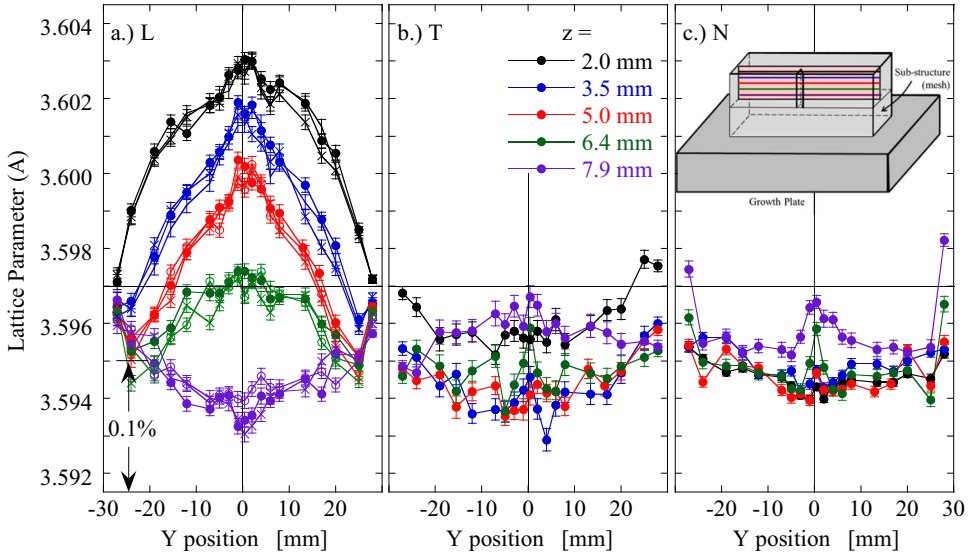

Fig. 5. (a)–(c) Longitudinal (y) line profiles of L, T, and N-direction lattice parameters on an y-z plane (at x=3.8 mm) at increasing values of z. z=10 mm is at the interface with the mesh sub-structure and z=0 mm is the free surface. (a) includes data from samples C (solid circles), D (open circles) and K (x's). (b) and (c) only include data from sample C. The inset schematic in (c) highlights the locus of measurement points (colors matched to plots) on the specimen. (For interpretation of the references to color in this figure legend, the reader is referred to the web version of this article.)

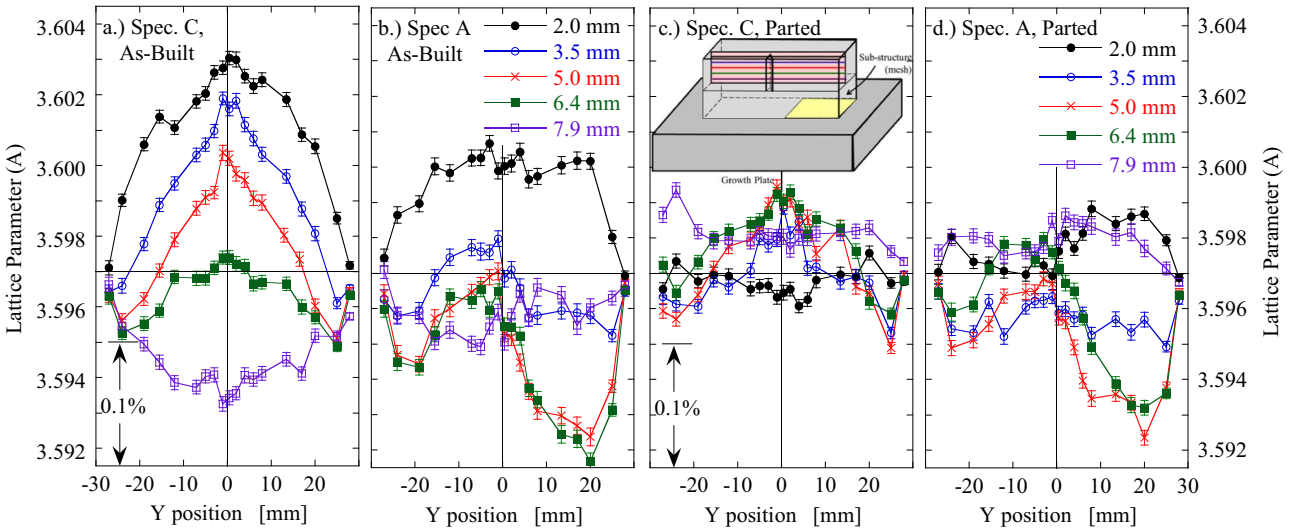

Fig. 6. (a)–(d) Longitudinal (y) line profiles of L-direction lattice parameters on an y-z plane (at x=3.8 mm) at increasing values of z. z=10 mm is at the interface with the mesh sub-structure and z=0 mm is the free surface. a and b (c and d) include data from Specimen C and A before (after) parting from the support structure. The inset schematic in (c) highlights the locus of measurement points (colors matched to plots) on the specimen. The yellow area represents the approximate location of the tear in Specimen A. (For interpretation of the references to color in this figure legend, the reader is referred to the web version of this article.)

deposited on the free surface (z=0). As it cools, this material tries to shrink but is constrained by the cooler, rigid material closer to the interface. The cooling material is pulled into a large residual tensile stress, while the already cold (relatively) material is squeezed into compression. The constraint of the relatively cold, previously deposited material is again apparent in the T stresses as they are also tensile at the free surface and compressive near the interface. However, based on the relative magnitudes of the L and T stresses it is apparent that the geometry of the part plays a controlling role in the development of the stress. That is, the larger stress component is that parallel to the longest in-plane direction of the sample. Also, the N stresses are relatively small compared to L stresses. This is distinct from previously reported stresses on parts with a similar geometry (an L-shape rather than straight, but similar aspect ratios) grown with powder bed deposition directly on a solid base plate using the Concept scheme [9] in which the peak N stresses were ~2x the in-plane stresses.

This is a common stress profile observed in welds. AM is distinct from welding in that many layers are built successively, where welds are generally limited to a few material passes. This leads one to question the development of the residual stress state in early deposited layers as the build continues. Presumably, early layers also experience a tensile longitudinal residual stress immediately after deposition. However, as subsequent layers are added, the early layers experience thermal profiles which may well anneal them. Also, the early layers will perceive compressive stress from the shrinkage of newly applied layers. Thus, it seems likely that the early layers will initially be in a state of tensile stress and evolve to the observed compressive stress, but evolution of stresses in the early layers will only be understood with in-situ measurements, or measurements taken at multiple stages of the same build, which will be attempted in the future.

It should be noted that the current data cannot be used to determine the stress closer than 2 mm from the sample surface. At z=2 mm, the residual longitudinal stress is 400 MPa and increasing rapidly as the free surface is approached. The L stress could be much larger at the surface. The observed stresses are more than 2/3's of the observed yield strength of the as-deposited material, and likely approach the yield strength at the surface.

As the L and T lattice parameter measurements in Samples D and K were identical (with uncertainty) to Sample C, it is reasonable to assume that the stresses are equivalent. It is surprising that changing the fragmentation and hatching of the sub-structure mesh did not appreciably affect the residual stress of the as-built samples as the amount of connectivity between the sample and growth plate must control the thermal conductivity out of the growing sample as well as the mechanical constraint of the sample.

Fig. 9(b) shows a similar stress map observed on Sample A. Recall that the sub-structure of Sample A was partially separated from the base plate. The extent of the tear (from y=~0–20 mm) is indicated schematically in the figure. The resulting residual stress profile lacks the symmetry in the y-direction exhibited by Sample C. The tensile stress on the top surface is considerably reduced relative to Sample C, but a significant compressive stress (~−400 MPa) is present near the center height (z=5–7 mm) of the sample directly over the tear.

Fig. 9(c) and (d) again show stress maps on Samples A and C, but this time after parting from the growth plate and sub-structure. In each case, the residual stresses relax significantly (bounded by roughly ± 200 MPa) following removal. The L stresses in sample C become more symmetric about the center height of the sample, now tensile (slightly) near the previously constrained surface, and compressive on the top. Like the L stresses, the in-plane stresses also re-distribute and become more symmetric about the center height after parting from the base plate. The N stresses are significantly relaxed after parting from the

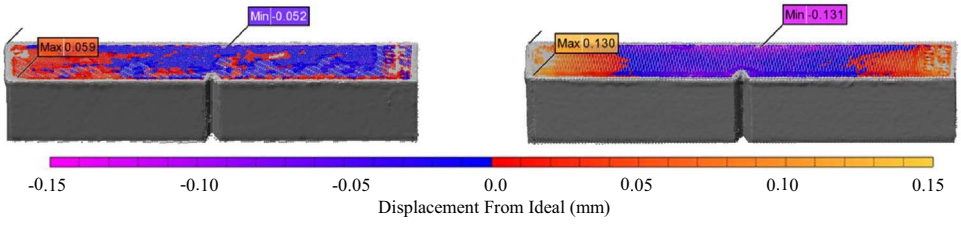

Fig. 7. (a) and (b) Displacement of top surface of Charpy specimen M from ideal defined by the CAD drawing before and after removal from the base plate and substructure. (For interpretation of the references to color in this figure legend, the reader is referred to the web version of this article.)

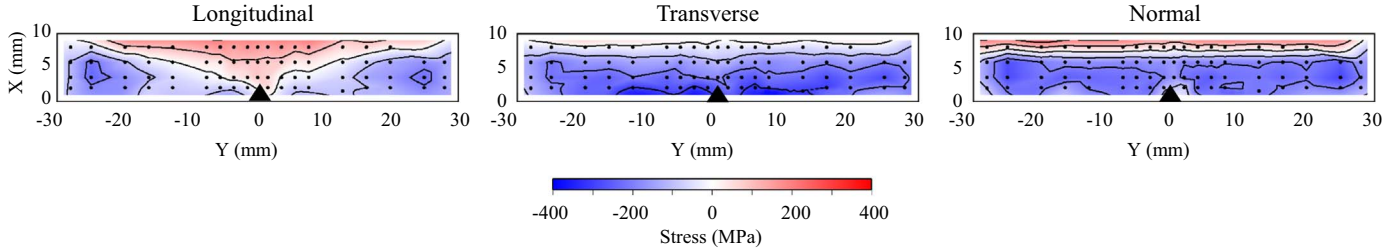

Fig. 8. Contour plots of L, T, and N-direction stresses, respectively, on an x-y plane (at z=5.0 mm) in sample C while still attached to sub-structure and growth plate. Points represent actual measurement positions. The solid black triangle roughly represents the location of the notch. Contours range from −400 to 400 MPa at intervals of 100 MPa (red is tensile, blue compressive). The white area outside of the contours but inside the boundary represent material inaccessible to neutron diffraction measurements.

build plate.

The observed relaxation of the L component of the stress is consistent with the distortion observed following removal of the specimen from the base plate and sub-structure (see Fig. 7). In particular, the ends of the sample bend up when removed from the base plate, consistent with the observed release of the bending moment in the L component of the residual stress (Fig. 9(a) and (c). Moreover, the broader and deeper depression in the surface on the side opposite the notch closely matches the x-y plane stress profile shown in Fig. 8.

Following removal of Sample A from the build plate, the tensile L stresses at z=2 mm again relax, but the asymmetry and significant compressive stress remain above location of the original tear. The presence of the separation between the sub-structure and base plate clearly alters the final residual stress in the part relative to the sample that remained intact.

It is clear that the tear in Sample A was not present in the size seen in Fig. 2(b) during the fabrication sequence as the distortion would have interfered with the recoater arm action. It was considered that the tear in Sample A may have happened after completion of the build. Then, the tear could be considered as an initial stage of the parting processes. In other words, Sample A could be thought of as an intermediate state between Sample C as-deposited and after removal, and the residual stresses in Sample A and C would be similar following completion of the parting operation. However, this is not the case as the final residual stresses in Sample A are very different.

Thus, we conclude that the tear occurred during the build and opened incrementally with increased deposition layers such that at no point was the incremental distortion enough to interfere with the recoater arm. Clearly, local removal of the conduction of heat and mechanical constraint from the growth plate due to the tear alters the residual stress state during its fabrication. The asymmetry in stress state, introduced by asymmetrical thermal transport due to the tear, propagates through to the final state of the sample. The permanent, asymmetrical stress state, strongly suggests that the tear was present throughout the fabrication sequence.

5. Conclusions

Neutron diffraction was used to determine residual stress in several additively manufactured GP-1 stainless steel samples with a Charpy test specimen geometry. The notch in the geometry inserted a transverse asymmetry to the stress field in the samples that remained through removal of the part from the growth plate. The largest observed residual stresses are in the longitudinal direction and are greater than half of the observed yield point (~400 MPa tensile and compressive) of the as-deposited material. The residual stresses do not depend appreciably on the hatching or fragmentation over the limited range sampled in this study. Significant redistribution of stress is apparent when parted from the growth plate and sub-structure, accompanied by significant distortion of the sample from the as-built

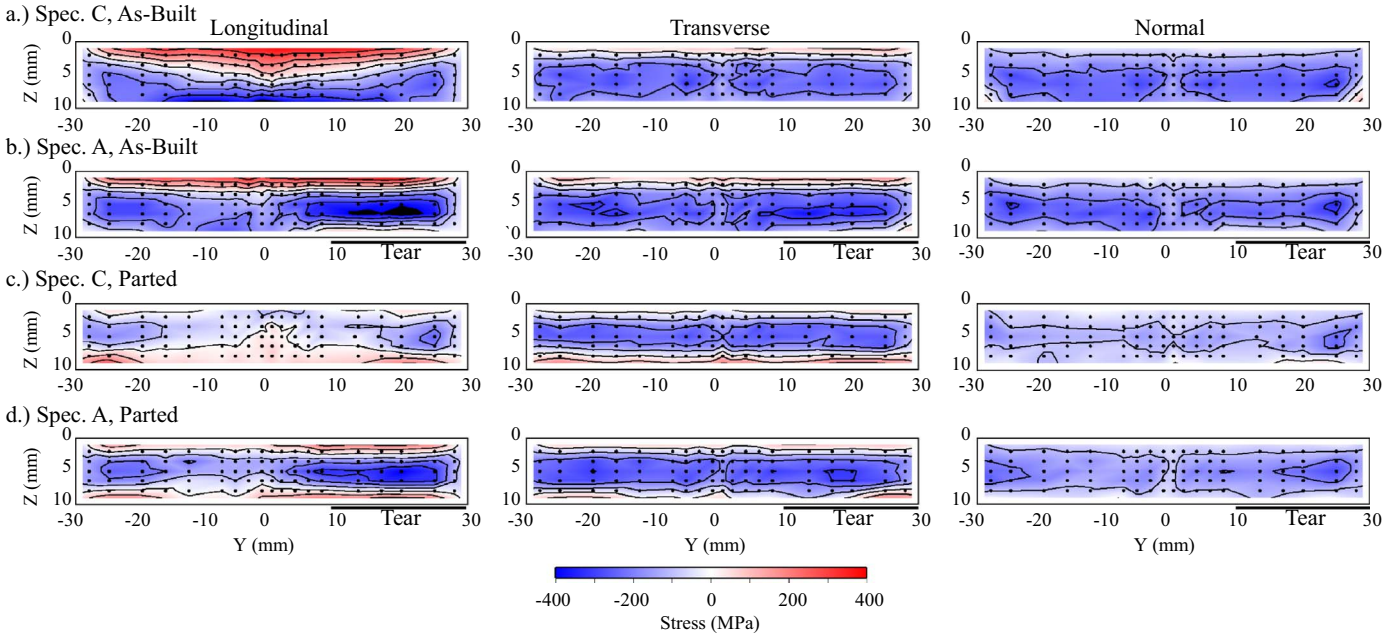

Fig. 9. (a)–(d) (a) and (b) Contour plots of L, T, and N-direction stresses, respectively, on an y-z plane (at x=3.8 mm) in sample C and A, respectively, while still attached to sub-structure and growth plate. (c) and (d) Similar contour plots after removal from the sub-structure and growth plate. Points represent actual measurement positions. Contours range from −400 to 400 MPa at intervals of 100 MPa (red is tensile, blue compressive). The white area outside of the contours but inside the boundary represent material inaccessible to neutron diffraction measurements. (For interpretation of the references to color in this figure legend, the reader is referred to the web version of this article.)

shape. A tear that occurred between the growth plate and sub-structure on one of the samples had a strong effect on the residual stresses which propagated through the parting operation to the final state of the sample. These data provide a wealth of information towards development and validation of computational modeling of the additive manufacture process.

Acknowledgements

Los Alamos National Laboratory, an affirmative action equal opportunity employer, is operated by Los Alamos National Security, LLC, for the National Nuclear Security Administration (NNSA) of the U.S. Department of Energy under contract DE-AC52-06NA25396. The authors gratefully acknowledge the financial support of the Los Alamos Neutron Science Center by the NNSA.

References

[1] P. Mercelis, J.P. Kruth, Rapid Prototyp. J. 12 (2006) 254–265.
[2] J.P. Jarvinen, V. Matilainen, X. Li, H. Piili, A. Salminen, I. Makela, O. Nyrhila, Phys. Procedia 56 (2014) 72–81.
[3] C.J. Smith, F. Derguti, E.H. Nava, M. Thomas, S. Tammas-Williams, S. Culizia, D. Fraser, I. Todd, J. Mater. Process. Technol. 229 (2016) 128–138.
[4] A. Hussein, L. Hao, C. Yan, R. Everson, P. Young, J. Mater. Process. Technol. 213 (2013) 1019–1026.
[5] G. Strano, L. Hao, R.M. Everson, K.E. Evans, Int. J. Adv. Manuf. Technol. 66 (2013) 1247–1254.
[6] A. Riemer, S. Leuders, M. Thoene, H.A. Richard, T. Troester, T. Niendorf, Eng. Fract. Mech. 120 (2014) 15–25.
[7] I. Yadroitsev, I. Yadroitsava, Virtual Phys. Prototyp. 10 (2015) 67–76.
[8] B.A. Szost, S. Terzi, F. Martina, D. Boisselier, A. Prytuliak, T. Pining, M. Hofmann, D.J. Jarvis, Mater. Des. 89 (2016) 559–567.
[9] A.S. Wu, D.W. Brown, M. Kumar, G.F. Gallegos, W.E. King, Met. Trans. A 45A (2014) 6260–6270.
[10] T. Watkins, H. Bilheux, K. An, A. Payzant, R. Dehoff, C. Duty, W. Peter, C. Blue, C. Brice, Adv. Mater. Process. 171 (2013) 23–27.
[11] T.GnaeupelHeroldJ.SlotwinskiS.Moylan, Neutron measurements of stresses in a test artifact produced by laser-based additive manufacturing, in: D.E. Chimenti, L.J. Bond, D.O. Thompson (Eds.), Proceeding of the 40th Annual Review of Progress in Quantitative Nondestructive Evaluation: Incorporating the 10th International Conference on Barkhausen Noise and Micromagnetic Testing, 2014 vol. 33a & 33b, pp. 1205–1212.
[12] A.D. Krawitz, Mater. Sci. Technol. 27 (2011) 589–603.
[13] D.W. Brown, M.A. Okuniewski, B. Clausen, G.A. Moore, T.A. Sisneros, J. Nucl. Mater. 474 (2016) 8–18.
[14] D.R. Haeffner, J.D. Almer, U. Lienert, Mater. Sci. Eng. A 399 (2005) 120–127.
[15] D.W. Brown, M.A. Okuniewski, J.D. Almer, L. Balogh, B. Clausen, J.S. Okasinski, B.H. Rabin, J. Nucl. Mater. 441 (2013) 252–261.
[16] ASTM, Standard Test Methods and Definitions for Mechanical Testing of Steel Products, ASTM International, West Conshohocken, PA, 2015.
[17] M.A.M. Bourke, D.C. Dunand, E. Ustundag, Appl. Phys. A A74 (2002) S1707–S1709.
[18] R.B. Vondreele, J.D. Jorgensen, C.G. Windsor, J. Appl. Crystallogr. 15 (1982) 581–589.
[19] M.R. Daymond, J. Appl. Phys. 96 (2004) 4263–4272.
[20] T.LorentzenT.Leffers, in: H.Fujiwara, T. Abe, K. Tanaka (Eds.), Proceeding of the 3rd International Conference on Residual Stresses (ICRS-3), Tokushima, Japan, Elsevier Applied Science, London and New York, 1992, pp.1063–1068.
[21] EOS, Material Data Sheet, EOS GP1, ⟨http://www.eos.info/material-m⟩, 2016.